

Regularization Imaging Algorithm with Accurate G Matrix for Near-Field MMW Synthetic Aperture Imaging Radiometer

Jianfei Chen¹, Yuehua Li^{1, *}, Jianqiao Wang¹, Yuanjiang Li^{1, 2}, and Yilong Zhang¹

Abstract—In order to improve the reconstruction accuracy of near-field SAIR, a novel regularization imaging algorithm based on an accurate G matrix is proposed in this paper. Due to the fact that the regularization reconstruction is usually an underdetermined problem, inaccurate operation matrix G will lead to great reconstruction error in the imaging results, or even the normal imaging cannot be obtained. In this paper, we establish an accurate G matrix based on the accurate imaging model of near-field SAIR. Compared with the traditional G matrix with some unnecessary approximations, the proposed G matrix without approximation can improve the reconstruction accuracy effectively. For improving the accuracy of matrix G further, the corresponding parameters are corrected according to the RMSE between the imaging results of the regularization method and modified FFT method which is not sensitive to the parameters' change. The effectiveness of this calibration method has been tested by 1D simulation experiments. Moreover, the 2D simulation experiments demonstrate that the proposed accurate G matrix can improve the imaging accuracy of regularization method effectively. Finally, the 1D imaging experiment is performed to test the effectiveness of the proposed method for the actual synthetic aperture imaging further.

1. INTRODUCTION

Due to the fact that the millimeter wave (MMW) radiation (30 ~ 300 GHz) is harmless to humans and is able to penetrate through most dielectric materials such as clothing, cardboard, plastics, and wood with comparatively trifling loss, the MMW imaging is a powerful tool for the detection of objects concealed under clothing [1, 2]. High resolution image can also be easily achieved by the MMW imaging system with the shorter wavelength. With these abilities, MMW imaging has been used in a variety of applications including target surveillance and precision target imaging for military purposes, safe aircraft landing, highway traffic monitoring in fog, remote sensing for civil applications and concealed threat object detection for security concerns [3–5].

Among the MMW imaging systems, the synthetic aperture imaging radiometer (SAIR) is one of the most popular systems as a result of increasing demand for high resolution imaging. Different from the traditional real-aperture imaging systems, SAIR uses a thin array composed of small aperture antennas to achieve large antenna aperture for solving the contradiction between the antenna aperture and spatial resolution. Then the visibility functions, which are the spatial Fourier transform of the brightness temperature distributions [6], are measured by performing correlation operations between each antenna pair. Obviously, the brightness temperature images can be acquired by the fast Fourier transform (FFT) from the visibility functions directly. However, the complete visibility functions distributed in the rectangular grid are required for FFT methods. Unfortunately, the rectangular visibility functions

Received 16 January 2014, Accepted 24 February 2014, Scheduled 25 February 2014

* Corresponding author: Yuehua Li (nlglyh2013@sina.cn).

¹ School of Electronic Engineering and Optoelectronic Technology, Nanjing University of Science and Technology, Nanjing 210094, China. ² Institute of Electronic and Information, Jiangsu University of Science and Technology, Zhenjiang 212000, China.

only can be measured by a few regular antenna arrays with serious baseline redundancy (such as the “T”, “U” and “L” arrays). For utilizing the antennas more effectively, the antenna arrays used in the actual SAIR are irregular sparse arrays with fewer redundancy baselines, such as the “Y” array, rotation array, hexagonal and non-redundant arrays [7–9]. Generally, the visibility functions measured by these irregular sparse arrays are non-uniform. Furthermore, the size of the brightness temperature image is usually larger than the visibility function in actual imaging. Clearly, the FFT-based methods are powerless for SAIR to reconstruct the images from the non-uniform visibility functions directly. For solving this predicament of the FFT-based methods, the hexagonal FFT and the Gridding methods are used for the SAIR. But, the hexagonal FFT is only suitable for the “Y” and triangle array with the special hexagonal visibility distribution [6]. And for the Gridding methods, the non-uniform visibility functions are first re-sampled from the irregular grid onto the rectangular grid by interpolations [10–12]. Then the images are reconstructed by the FFT-based methods from the re-sampled visibility functions. But many additional errors are attached to the re-sampled visibility functions when the interpolation and resample are applied, and these errors are difficult to be removed.

In 1990s, Lannes et al. pointed out that the regularization could be used for reconstructing the MMW images of SAIR from the non-uniform visibility functions accurately, and the satisfying recovery effects were achieved [13, 14]. Because regularization reconstructions of the SAIR with sparse arrays are an underdetermined problem, the accuracy of operation matrix G is very important for the reconstruction process. Now, the matrixes G s are mostly established from the forward analysis of SAIR imaging process [15–18]. For the purpose of variables separation, some unnecessary approximations are adopted to simplify the G matrixes in different degrees. In order to improve the accuracy of the regularization reconstruction further, we establish an accurate G matrix without non-essential approximation based on the accurate imaging model of near-field SAIR in this paper. The corresponding parameters are then corrected according to the root-mean square error (RMSE) between the imaging results of the reconstruction method and modified FFT method. Because only the phase-modified item is added to the FFT, which can be seen as the focusing operation for the MMW SAIR [17–19], the modified FFT method (one kind of the FFT-based methods) is insensitive to the change of those corresponding parameters. For verifying the effectiveness of the proposed accurate G matrix, the traditional regularization with the approximate G matrix is also tested for comparison. The numerical simulation results demonstrate that the proposed regularization method with an accurate G matrix can improve the imaging accuracy effectively. Finally, the 1D imaging experiment is performed to test the effectiveness of the proposed method further. Moreover, the proposed parameters calibration method can also be utilized to estimate the system parameters by comparing the RMSEs between the regularization methods and modified FFT method.

2. THE REGULARIZATION METHOD BASED ON AN ACCURATE G MATRIX

2.1. An Accurate G of Near-Field MMW SAIR

For establishing the matrix G accurately, the theory of near-field MMW synthetic aperture imaging is re-derived firstly. As Fig. 1 shows, the extend radiation source S is located on oxy , and the antennas are located on OXY . The radiation source S is dispersed into N small parts. The distances between the n -th radiation source S_n and antennas c and l are R_n^c and R_n^l , respectively.

According to [6], the visibility sample of each antenna pair (c - l) can be expressed as

$$V_{c,l} = \left\langle E_c(R_n^c, t) \cdot E_l^*(R_n^l, t) \right\rangle_\tau = \sum_{n=0}^M T(x_n, y_n) F_c(x_n, y_n) F_l^*(x_n, y_n) r_{c,l} \exp \left[-jk(R_n^c - R_n^l) \right] \quad (1)$$

where $E_\#(\cdot)$ is the received electromagnetic signal of antenna $\#$, $\langle \cdot \rangle$ the time integration operation, τ the integration time, (x_n, y_n) the coordinate of the n -th radiation source S_n , $T(x_n, y_n)$ the normalized brightness temperature, $F_\#(\cdot)$ the normalized antenna pattern of antenna $\#$, $k = 2\pi/\lambda$ the circular wave number, λ the center wavelength of SAIR, and $r_{c,l}$ the fringe-wash function. Generally, the decorrelation effects are negligible, and $r_{c,l} = 1 \cdot \exp[-jk(R_n^c - R_n^l)]$ is the phase difference of two antennas, which is the key factor for synthetic aperture imaging. According to Fig. 1, the distances R_n^c and R_n^l can be

expressed as

$$R_n^c = \sqrt{(x_n - X_c)^2 + (y_n - Y_c)^2 + R^2} \tag{2}$$

$$R_n^l = \sqrt{(x_n - X_l)^2 + (y_n - Y_l)^2 + R^2} \tag{3}$$

For the purpose of the variables separation, the distances R_n^c and R_n^l are usually unfolded by the Taylor expansion approximately [6, 7, 16–19]. Then the difference between R_n^c and R_n^l can be expressed as

$$\begin{aligned} \Delta R_{n,c,l} &= R_n^c - R_n^l \approx \left(R + \frac{(x_n - X_c)^2 + (y_n - Y_c)^2}{2R} \right) - \left(R + \frac{(x_n - X_l)^2 + (y_n - Y_l)^2}{2R} \right) \\ &= \frac{x_n(X_l - X_c) + y_n(Y_l - Y_c)}{R} + \frac{(X_c^2 + Y_c^2) - (X_l^2 + Y_l^2)}{2R} \end{aligned} \tag{4}$$

In the far-field imaging ($R \gg D_{SA}$, D_{SA} is the antenna aperture of SAIR), and the second item is similar to 0 and usually omitted. But in the near-field imaging, this is the so called phase-modified item which is the key for the near-field imaging. Substituting Eq. (4) into Eq. (1), we can get the approximate matrix G_{ap} and the modified FFT imaging formula as follows [17, 19].

$$G_{ap}(m, n) = F_c(x_n, y_n)F_l^*(x_n, y_n)e^{j\pi[2x_n(X_{mc}-X_{ml})+2y_n(Y_{mc}-Y_{ml})+X_{ml}^2+Y_{ml}^2-X_{mc}^2-Y_{ml}^2]/R\lambda} \tag{5}$$

$$T^{MF}(x, y) = FT_2 \left[e^{j\varphi(v,h)}V(v, h) \right] \tag{6}$$

where (X_{mc}, Y_{mc}) and (X_{ml}, Y_{ml}) are the coordinates of antenna pairs ($c-l$), the corresponding visibility sample is V_m , T^{MF} is the reconstructed image of modified FFT method, $FT_2[\cdot]$ denotes the 2D Fourier transform, $V(v, h)$ is the visibility function and $v = k(X_l - X_c)/R$, $h = k(Y_l - Y_c)/R$, $\varphi(v, h) = k(X_c^2 + Y_c^2 - X_l^2 - Y_l^2)/2R$.

However, we find that the approximations of ΔR (such as Eq. (4)) are unnecessary for the regularization method without the variables separation in near-field SAIR. Thus, an accurate matrix G_{ac} can be acquired according to Eq. (2) and Eq. (3) directly.

$$G_{ac}(m, n) = F_c(x_n, y_n)F_l^*(x_n, y_n)e^{j\pi(\sqrt{(x_n-X_{ml})^2+(y_n-Y_{ml})+R^2}-\sqrt{(x_n-X_{mc})^2+(y_n-Y_{mc})+R^2})/\lambda} \tag{7}$$

Then the visibility integral of Eq. (1) can be rewritten into the following linear matrix equation.

$$V_{M \times 1} = G_{M \times N}T_{N \times 1} \tag{8}$$

where $V_{M \times 1}$ is the measured near-field visibilities, $T_{N \times 1}$ the original brightness image, and $G_{M \times N}$ the coefficient matrix, which characterizes the system configuration and objects spatial distribution (such as Eq. (5) and Eq. (7)).

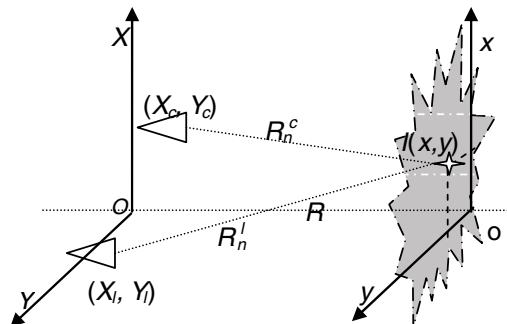


Figure 1. Interference measurement schematic.

2.2. Regularization Reconstructions for the Near-Field SAIR

A straightforward solution to the inverse problem of Eq. (8) is given by the Moore-Penrose pseudo-inverse.

$$T = G^H (GG^H)^{-1} V \quad (9)$$

However, because sparse arrays are usually utilized in the actual millimeter wave SAIR, the dimensions of visibility functions (V) are significantly less than the ones of brightness temperature matrix (T). So the matrix equation Eq. (8) is an underdetermined equation with underdetermined G matrix, and we cannot acquire a unique and stable solution by the straightforward method of Eq. (9). Besides, the dominant noises in SAIR images are usually the Gaussian white noises. Under this circumstance, the regularization is one of the most effectual methods to estimate the unique and stable T^R , and the satisfying recovery effects are achieved in near-field imaging [18, 19]. In this paper, we estimate T^R by minimizing the following function.

$$\begin{cases} T^R = \min_T E(T) \\ E(T) = \|V - GT\|_F^2 + \alpha P(T) \end{cases} \quad (10)$$

where $\|V - GT\|_F^2$ is the fidelity term, which guarantees that the difference between actual visibility function and the observation visibility function is small enough. $P(T)$ is the penalty function or the constraint condition item and α the regularization parameter, which is used to balance the fidelity term and regularization term. Usually α is set small enough for maintaining the superior spatial resolution of MMW images. The penalty term $P(T)$ can be written as [20]

$$P(T) = \sum_{n=1}^N \frac{1}{2} \sum_{k \in K_n} w_{kn} \varphi(T_n - T_k) \quad (11)$$

where K_n is a neighborhood of pixels near pixel n , $\varphi(T)$ a symmetric convex function, and $w_{nk} = w_{kn}$. To be simple, the quadratic penalty function ($\varphi(T) = T^2/2$) is adopted in this paper. Numerous optimization methods can be used to solve the problem of Eq. (10) [21–24]. In this paper, we use the fast proximal-gradient projection algorithm (FGP) [23] with the accelerated convergence rate $O(k^{-2})$ to solve Eq. (10).

2.3. Parameters Calibration for the G Matrix

The main parameters of the matrix G (such as G_{ac} and G_{ap}) are R and λ . Compared to the accurate λ determined by the MMW SAIR system, the parameter R with some errors is usually estimated by the experimenters in actual imaging applications. Clearly, the inaccuracy of parameter R is unacceptable in the regularized reconstruction and needs to be corrected. Due to the fact that the modified FFT is actually the 2D FFT after the phase compensation of visibility function (Eq. (6)), its imaging results are not sensitive to the change of those parameters. For evaluating the accuracies of the reconstructed images T_s , we define the RMSE as

$$RMSE(X, X_o) = \frac{\sqrt{\sum_i [X(i) - X_o(i)]^2}}{\sqrt{\sum_i X_o(i)^2}} \quad (12)$$

where X_o is the original reference image, and X is the reconstructed image needs to be evaluated. However, the accurate original images (T^A) are unable to be got in the actual MMW imaging. So the reconstructed images (T^{MF}) of modified FFT method are utilized to replace the original MMW images for evaluating the reconstruction accuracy of the regularization method and then correcting the parameter R or λ . The rationality of this method has been verified by the experiments demonstrated in Section 3.

Since the error of R is usually larger than the other G parameters, we mainly correct the parameter R in this paper. It is easy to be extended to the correction of other parameters (such as λ). The specific

correction method is as follows: We first calculate the $RMSE(T^R, T^{MF})$ with the different R from $0.5R_0$ to $1.5R_0$ (R_0 is the initial estimate value of R), then plot the change curve of $RMSE(T^R, T^{MF})$ with parameter R . We find that the change curve of $RMSE(T^R, T^{MF})$ with R are very similar to $RMSE(T^R, T^A)$, and the minimum values of them are almost appeared at the same R_a mostly. The corresponding R_a is the correct value of the parameter R , which meets the matching relation between the matrix G_{ac} and the actual imaging. Then the accurate images can be reconstructed by the regularization based on accurate G_{ac} with the correctional parameters. This method takes advantage of the characteristics of FFT-based methods and regularization methods, and these characteristics are their lacks formerly.

Compared with the conventional regularization algorithm, the superiorities of the proposed method are the employment of an accurate G_{ac} and the parameter calibration method. The main trade-off of the proposed method is the additional step of parameters calibration, which does not belong to the conventional regularization. For correcting the parameters quickly, the parameters calibration is usually performed in the 1D experiments with less data. Thus, the calculated amount of parameter calibration is less than the one of 2D regularization imaging (the solution of Eq. (10)), and this trade-off can be ignored in actual imaging applications.

3. THE EXPERIMENTS AND RESULTS

3.1. 1D Simulation Experiments

For evaluating the effectiveness of the parameter correction method mentioned in Section 2.3, the 1D simulation experiments with two different extended sources are performed here. Compared with the 2D experiments, 1D simulation experiments with less data are more suitable for finding an accurate R_a . The main simulation parameters of the 1D experiments are listed in Table 1.

Table 1. The main simulation parameters.

| Parameters | Center wavelength λ | Antenna array size | Antenna spacing Δd | Imaging distance R |
|------------|-----------------------------|--------------------|----------------------------|----------------------|
| Value | 8 mm | 50 | 0.01 m | 5 m |

The 50 antennas are placed into a straight line such as the X -axis of Fig. 1, and the step is 0.01 cm. The 1D target scenes are parallel to the X -axis such as x -axis of Fig. 1, and the spacing between radiation sources is set as the half of spatial resolution.

$$\Delta L = 0.5\rho = 0.5 \frac{\lambda}{D_{SA}} R = 4 \text{ cm} \quad (13)$$

where ρ is the spatial resolution of SAIR, $D_{SA} = P \cdot \Delta d = 0.5 \text{ m}$. Thus for a target scene with the size of 100, the corresponding dimension is 4 m which is equal to the size of no-aliasing FOV of this given SAIR. Due to the fewer visibility samples, the size of the results (T^{MF}) of modified FFT method is 50, which is only half of the regularization method. We need to extend it to 100 by the linear interpolation for comparing with the results of the regularization methods. This problem is not listed in the regularization methods. Under the same condition, the regularization with the matrix G_{ac} and G_{ap} are both tested for comparison, and their imaging results are T_{ac}^R and T_{ap}^R respectively. In these simulations, the parameter R is changing from $0.5R_0$ to $1.5R_0$ ($R_0 = 5 \text{ m}$), and the step is 0.05 m. The simulation results are shown in Figs. 2–3.

As the two group simulation results show, with the change of parameter R , the $RMSE(T^{MF}, T^A)$ of the modified FFT results (red dotted lines in Figs. 2–3(a)) are mostly invariable. However, due to the underdetermined matrixes (G_{ac} and G_{ap}), the RMSEs of the regularization methods change strongly with the change of R such as the magenta and blue dotted lines show. Moreover, the minimum $RMSE(T^{Rac}, T^A)$ are less than the $RMSE(T^{Rap}, T^A)$, which means that an accurate G_{ac} can improve the accuracy of the regularization method effectively. However, these RMSEs (the dotted lines) between

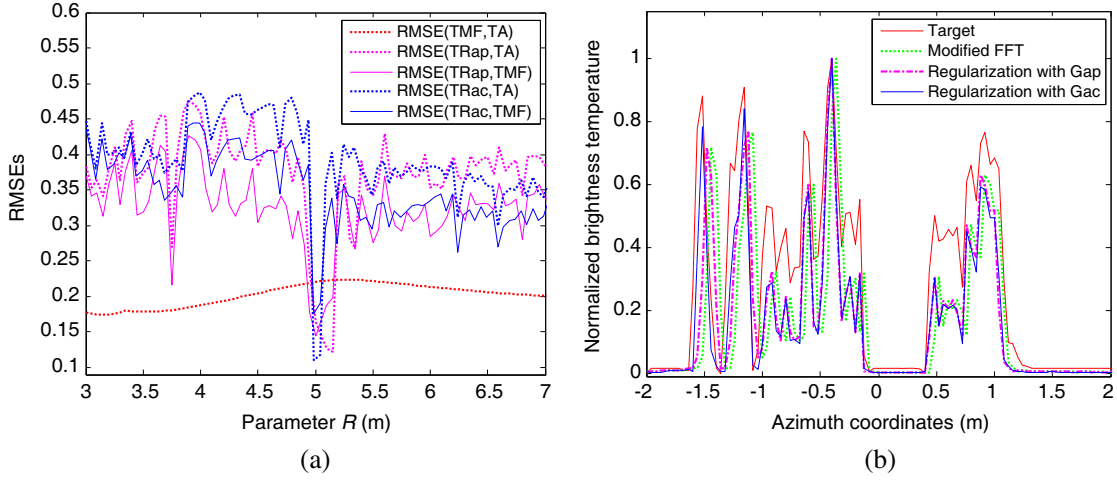


Figure 2. The reconstructed results of the three methods (Scene I). (a) The RMESs between the T^{MF} , T_{ap}^R , T_{ac}^R and T^A (the target). (b) The reconstructed results of the three methods with the accurate $R_a = 5$ m.

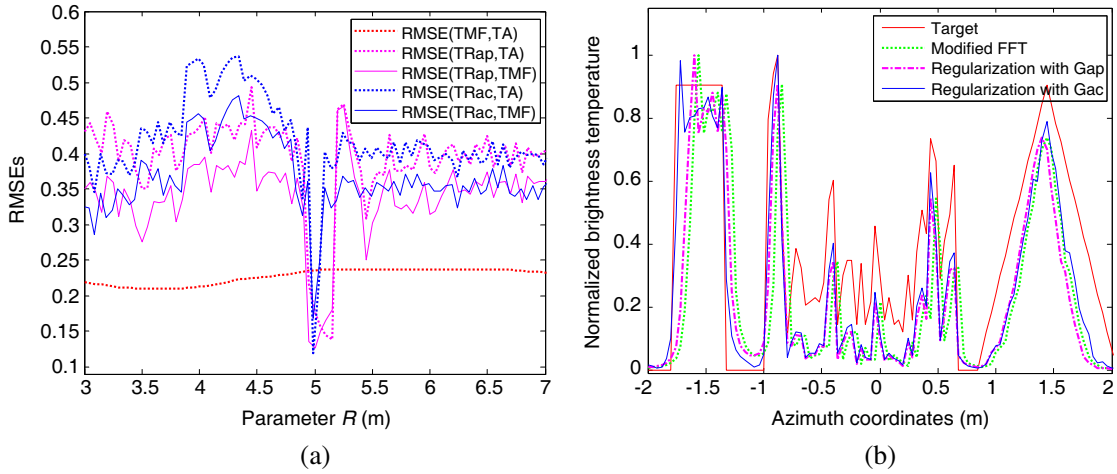


Figure 3. The reconstructed results of the three methods (Scene II). (a) The RMESs between the T^{MF} , T_{ap}^R , T_{ac}^R and T^A (the target). (b) The reconstructed results of the three methods with the accurate $R_a = 5$ m.

the reconstructed images and accurate original MMW image T^A are unable to be calculated, because we do not know the accurate MMW image T^A in practice. Thus we use the reconstructed images T^{MF} of modified FFT to instead of T^A to find the best R_{ac} . From Figs. 2–3(a), we can see that the change curve of $RMSE(T^{Rac}, T^{MF})$ and $RMSE(T^{Rap}, T^{MF})$ are very similar to that of $RMSE(T^{Rac}, T^A)$ and $RMSE(T^{Rap}, T^A)$, respectively. Moreover, the minimum values of them almost appear at the same R_a equal to actual imaging distance $R_0 = 5$ m. This means that we can use $RMSE(T^{Rac}, T^{MF})$ or $RMSE(T^{Rap}, T^{MF})$ to find an accurate R_a for improving the accuracy of G matrixes (G_{ac} and G_{ap}). Figs. 2–3(b) show the reconstructed images of the three methods with an accurate R_a . Clearly, the reconstructed images of the regularization methods are more accurate than that of modified FFT. The images reconstructed by the regularization method with G_{ac} are the best ones among the three methods, especially for the recovery of the targets located in the scene edge (such as the rectangular shows in Fig. 3(b)). In addition, due to the more accurate matrix G_{ac} used in the proposed method, the changes of $RMSE(T^{Rac}, T^A)$ are more severe than those of $RMSE(T^{Rap}, T^A)$ near R_a . This means that the proposed method is more sensitive to the parameters' change than the regularization methods with G_{ap} .

3.2. 2D Simulation Experiments

According to the 1D simulation experiments, we know that an accurate G_{ac} can improve the accuracy of the regularization method effectively. For evaluating this effectiveness in the image domain further, the 2D simulation experiments with three different scenes are performed here, and the structural similarity (SSIM) and peak signal-to-noise ratio (PSNR) are also used to evaluate the reconstructed images. The main simulation parameters are also set as Table 1.

For validating universality of the proposed method, a random sparse antenna array is used in the 2D simulation experiments. We first arrange 75 antennas to form the standard “T” antenna array with the size of 50×50 , and then add the random perturbations to each selected antenna coordinates to build the sparse antenna array. The maximum perturbation is 1 cm equal to the average antenna spacing. Fig. 4 shows that the distribution of the visibility function generated by the designed array has superior non-redundancy. The red points are antennas, and blue points are visibility samples.

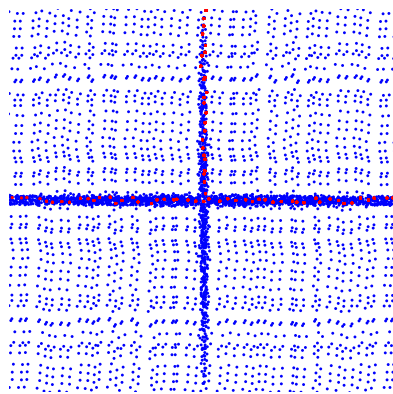


Figure 4. The distribution of the visibility functions measured by the random antenna array.

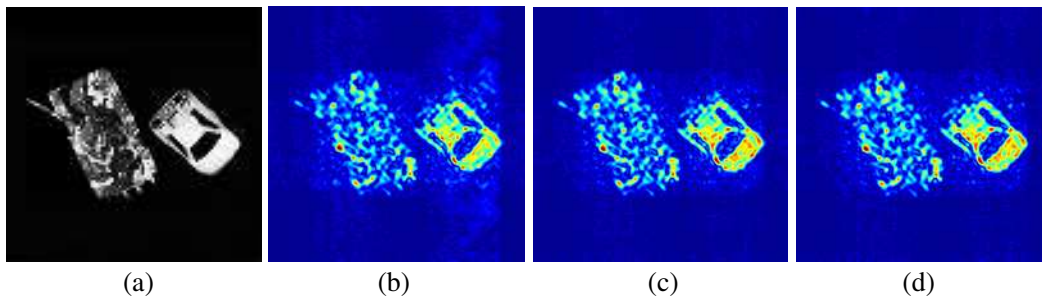


Figure 5. (b) The images reconstructed by modified FFT method. (c) The regularization method with G_{ap} and (d) the regularization method with G_{ac} . (a) The original image is tank&car.

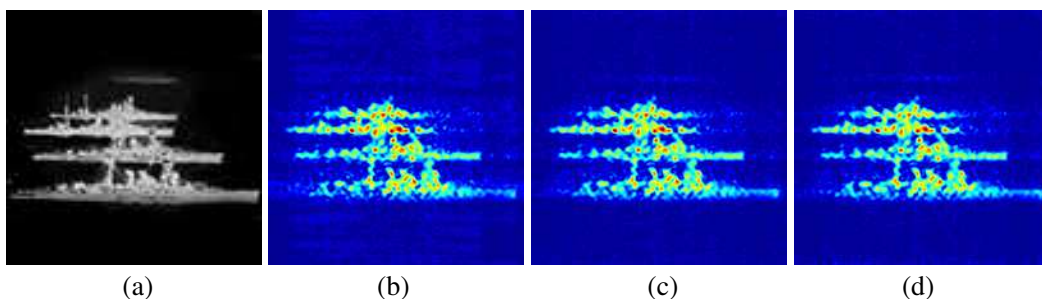


Figure 6. (b) The images reconstructed by modified FFT method. (c) The regularization method with G_{ap} and (d) the method regularization with G_{ac} . (a) The original image is boats.

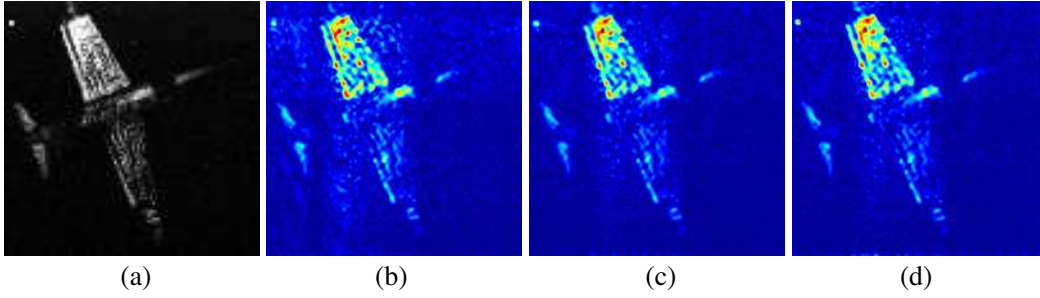


Figure 7. (b) The images reconstructed by modified FFT method. (c) The regularization method with G_{ap} and (d) the regularization method with G_{ac} . (a) The original image is airplane.

In order to simulate the SAIR imaging accurately, the received signals are gained by integral operation of the radiation waves generated by all discrete sources. The radiation intensities are set as the grey values according to the original images (Figs. 5–7(a)). The sizes of the target scenes are 100×100 , and the spacing between radiation sources is also set as 4 cm. The visibility samples are then calculated by cross-correlated calculation between each antenna pair. Clearly, the modified FFT method is unable to be utilized for these non-uniform visibility functions directly. So the Convolution Interpolation [10] is applied to resample the non-uniform visibility samples from the irregular grid onto the rectangular grid before using the modified FFT. But this problem is not listed in regularization methods, the MMW images can be reconstructed by the regularization methods directly. The simulation results are shown in Figs. 5–7.

From the above 2D simulation results, we can see that the modified FFT method is the worst one for reconstructing the MMW images from the non-uniform visibility functions. Even if the images can be reconstructed by using the interpolation algorithms, a lot of noise pollutions exist in its reconstructed images as shown in Figs. 5–7(b). And because the images are directly reconstructed from the original visibility samples by the regularization methods without interpolation, the noise pollutions of the reconstructed images (Figs. 5–7(c), (d)) are less than the results of modified FFT. Since many non-redundant samples measured by the random array (Fig. 4) are effectively used by the regularization methods, the images outlines of regularization methods seem to be clearer. Moreover, the accuracies of the images reconstructed by the regularization method with G_{ac} are better than those of regularization method with G_{ap} . For example, the tail of upper wing and the lightspot at upper-left shown in Fig. 7(d) are clearer than the ones in Fig. 7(c). For evaluating the accuracies of the three methods objectively, the PSNR and SSIM are calculated by the following formulas.

$$\text{PSNR}(T, T_o) = 10 \log_{10} \frac{\max(T_o)^2}{\sum_{0 < i < M, 0 < j < N} [T(i, j) - T_o(i, j)]^2 / M \times N} \quad (14)$$

$$\text{SSIM}(T, T_o) = \frac{(2\mu_T\mu_{T_o} + C_1)(\sigma_{TT_o} + C_2)}{(\mu_T^2 + \mu_{T_o}^2 + C_1)(\sigma_T^2 + \sigma_{T_o}^2 + C_2)} \quad (15)$$

where T is the reconstructed image and T_o the original one. μ_T and μ_{T_o} are the means of images T and T_o , respectively. σ_T and σ_{T_o} are the standard deviations of images T and T_o , respectively. σ_{TT_o} is the covariance of images T and T_o . C_1 and C_2 are the smallest positive constants. $\max(T_o)$ denotes the max value of the original image T_o .

The RMSEs, PSNRs and SSIM of the aforementioned three methods are calculated as shown in Table 2. Clearly, the RMSEs, PSNRs and SSIM of the regularization methods are all much better than those of modified FFT. Among the three methods, the RMSEs of regularization method with G_{ac} are the minimum ones, and its PSNRs and SSIM are the maximal ones. This means that an accurate G_{ac} can improve the reconstruction accuracy of regularization method effectively. Moreover, the improvement effects are clearer for the scenes with more targets located in the edge, just like the different values between the last two columns of Table 2 which are increasing with the change of scene from tank&car to airplane.

Table 2. Comparison of objective data among the three methods.

| Evaluation criterion and Scene | | Modified FFT | Regularization with G_{ap} | Regularization with G_{ac} |
|--------------------------------|-------------------|--------------|------------------------------|------------------------------|
| RMSEs | Tank&car (Fig. 5) | 0.0349 | 0.0341 | 0.0334 |
| | Boats (Fig. 6) | 0.0543 | 0.0539 | 0.0529 |
| | Airplane (Fig. 7) | 0.0506 | 0.0497 | 0.0458 |
| PSNRs | Tank&car (Fig. 5) | 17.0918 | 17.4571 | 17.4751 |
| | Boats (Fig. 6) | 16.8831 | 16.9457 | 16.9930 |
| | Airplane (Fig. 7) | 15.8246 | 16.2019 | 16.4666 |
| SSIM | Tank&car (Fig. 5) | 0.8819 | 0.9087 | 0.9101 |
| | Boats (Fig. 6) | 0.8904 | 0.8946 | 0.8991 |
| | Airplane (Fig. 7) | 0.5286 | 0.5876 | 0.6028 |

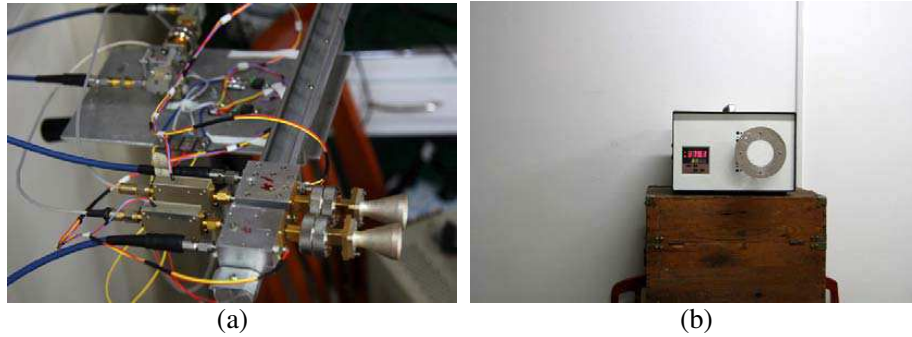


Figure 8. The scenarios of the 1D imaging experiment. (a) The binary interferometer. (b) The target scene with the 380° blackbody.

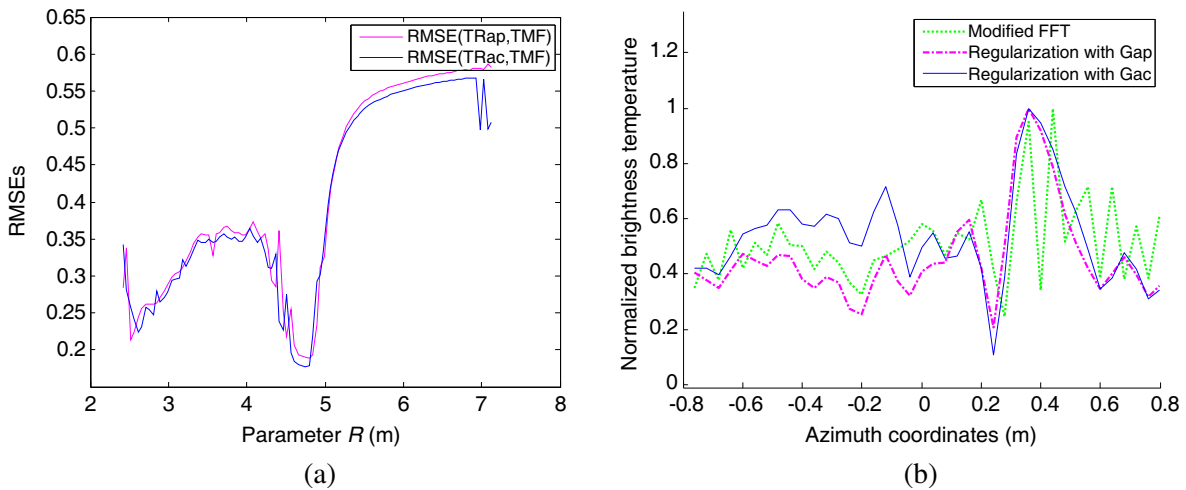


Figure 9. The 1D imaging experiment results. (a) The RMESs between the T^{MF} , T^{Rap} and T^{Rac} . (b) The reconstructed results of the three methods with the accurate $R_a = 4.71$ m.

3.3. 1D Imaging Experiment

Finally, we used the actual data measured by a simple binary interferometer to further test the proposed method. The experiment scenarios are shown in Fig. 8. The main parameters are as follows: center wavelength is 8.3 mm, antenna array is 20×1 , antenna spacing is 2.5 cm, and imaging distance is about

5 m.

As the above simulation experiments, we first find the optimum imaging distance R_a according to the $RMSE(T^{Rac}, T^{MF})$ and $RMSE(T^{Rap}, T^{MF})$. The corresponding calculated results are shown in Fig. 9(a). Clearly, the optimum distance is $R_a = 4.71$ m, which means that the estimated distance is inaccurate in this experiment. Then the 1D images are reconstructed by the three methods with the corrected R_a . Fig. 9(b) shows that the imaging results of the three methods are in agreement with each other as expected, and the correctness of the calibration method is also proved by this consistency. But due to the limit of the simple experimental equipment, only the rough images can be reconstructed from this few visibility samples which also have some errors. From the rough images, we can only find the blackbody in the right coarsely. Anyhow, the effectiveness of the proposed method is proved by this imaging experiment. The imaging prototype is being developed, and the 2D experiments may be done in the future.

4. CONCLUSION

In this paper, we show a regularization imaging method with an accurate G matrix for near-field MMW SAIR. Since regularization reconstruction is usually an underdetermined problem and very sensitive to the accuracy of the G matrix, we establish an accurate G matrix based on an accurate imaging model of near-field SAIR. Compared to the traditional G matrix, the proposed G matrix without unnecessary approximation can improve the reconstruction accuracy effectively. In order to improve the accuracy of the reconstructed MMW images further, the corresponding parameters of matrix G are corrected according to the RMSEs between the imaging results of the regularization method and modified FFT method. The effectiveness of the correction method has been verified by 1D experiments. Moreover, the 2D simulation experiments demonstrate that the superior improvement effect can be achieved by the proposed accurate G_{ac} by the comparison of the results between the regularization methods with G_{ac} and G_{ap} . Moreover, although the proposed method is presented for the near-field imaging of SAIR, it can also be utilized for the far-field imaging, and the superior reconstruction effects can be obtained.

ACKNOWLEDGMENT

The authors would like to thank the anonymous reviewer and editors for their helpful comments and suggestions. This work is supported by National (Jiangsu) Natural Science Foundation of China under Grants 61001010 and 60901008 (BK2010490), National Ministry Foundation of China under Grants 51305050102.

REFERENCES

1. Appleby, R. and R. N. Anderton, "Millimeter-wave and submillimeter-wave imaging for security and surveillance," *Proceedings of the IEEE*, Vol. 95, No. 8, 1683–1690, Aug. 2007.
2. Sheen, M. D., D. L. McMakin, and T. E. Hall, "Three-dimensional millimeter-wave imaging for concealed weapon detection," *IEEE Trans. Microwave Theory and Techniques*, Vol. 49, No. 9, 1581–1592, Sep. 2001.
3. Appleby, R., D. A. Wikner, R. Trebits, and J. L. Kurtz, "Mechanically scanned real-time passive millimeter-wave imaging at 94 GHz," *Proceedings of the IEEE*, Vol. 5077, 1–6, 2003.
4. Chen, H.-M., S. Lee, R. M. Rao, M. A. Slamani, and P. K. Varshney, "Imaging for concealed weapon detection: A tutorial overview of development in imaging sensors and processing," *IEEE Signal Processing Magazine*, Vol. 22, No. 2, 52–61, Mar. 2005.
5. Fetterman, M. R., J. Grata, G. Jubic, W. L. Kiser, Jr., and A. Visnansky, "Simulation, acquisition and analysis of passive millimeter-wave images in remote sensing applications," *Optics Express*, Vol. 16, No. 25, 20503–20515, Dec. 2008.
6. Camps, A., J. Bara, I. C. Sanahuja, and F. Torres, "The processing of hexagonally sampled signals with standard rectangular techniques: Application to 2-D large aperture synthesis interferometric radiometers," *IEEE Trans. Geosci. & Remote Sens.*, Vol. 35, No. 1, 183–190, Jan. 1997.

7. Tanner, B. A., H. B. Lambrigsten, M. T. Gaier, and F. Torres, "Near field characterization of the GeoSTAR demonstrator," *Proceedings of IEEE Geosci. Remote Sens. Symp.*, Denver, Co, USA, Jul. 2006.
8. Lucotte, B. M., B. Grafulla-Gonzalez, and R. A. Harvey, "Array rotation aperture synthesis for short range imaging at millimeter wavelengths," *Radio Science*, Vol. 44, No. 1, RS1006 1–11, 2009.
9. Mait, J. N., D. R. Martin, A. C. Schuetz, and W. D. Prather, "Millimeter wave imaging with engineered point spread functions," *Optical Engineering*, Vol. 51, No. 9, 091606-1, May 2012.
10. Rasche, V., R. Proksa, R. Sinkus, P. Bornert, and H. Eggers, "Resampling of data between arbitrary grids using convolution interpolation," *IEEE Trans. Medical Imaging*, Vol. 18, No. 5, 385–392, May 1999.
11. Fessler, J. A. and P. B. Sutton, "Nonuniform fast Fourier transforms using min-max interpolation," *IEEE Trans. Signal Processing*, Vol. 51, No. 2, 560–574, Feb. 2003.
12. Beatty, P. J., G. D. Nishimura, and M. J. Pauly, "Rapid gridding reconstruction with a minimal oversampling ratio," *IEEE Trans. Medical Imaging*, Vol. 24, No. 6, 799–808, Jun. 2005.
13. Lannes, A., E. Anterrieu, and K. Bouyoucef, "Fourier interpolation and reconstruction vis Shannontype techniques; Part I: Regularization principle," *J. Modern Opt.*, Vol. 41, No. 8, 1537–1574, 1994.
14. Lannes, A., E. Anterrieu, and K. Bouyoucef, "Fourier interpolation and reconstruction vis Shannon type techniques; Part II: Technical developments and applications," *J. Modern Opt.*, Vol. 43, No. 1, 105–138, 1996.
15. Picard, B. and E. Anterrieu, "Comparison of regularized inversion methods in synthetic aperture imaging radiometry," *IEEE Trans. Geosci. & Remote Sens.*, Vol. 43, No. 2, 218–224, Feb. 2005.
16. Camps, A., J. Bar'a, F. Torres, and I. Corbella, "Extension of the CLEAN technique to the microwave imaging of continuous thermal sources by means of aperture synthesis radiometers," *Progress In Electromagnetics Research*, Vol. 18, 67–83, 1998.
17. Zhang, C., J. Wu, H. Liu, and Y. J. Yan, "Imaging algorithm for synthetic aperture interferometric radiometer in near field," *Science China Technological Sciences*, Vol. 54, No. 8, 2224–2231, Aug. 2011.
18. Yao, X., C. Zheng, J. Zhang, B. Yang, A. Hu, and J. Miao, "Near field image reconstruction algorithm for passive millimeter-wave imager bhu-2D-u," *Progress In Electromagnetics Research C*, Vol. 45, 57–72, Oct. 2013.
19. Chen, J., Y. Li, J. Wang, Y. Li, and Y. Zhang, "An accurate imaging algorithm for millimeter wave synthetic aperture imaging radiometer in near-field," *Progress In Electromagnetics Research*, Vol. 141, 517–535. Aug. 2013.
20. Fessler, J. A. and W. L. Rogers, "Spatial resolution properties of penalized-likelihood image reconstruction methods: Space-invariant tomographs," *IEEE Trans. Imag. Process.*, Vol. 5, No. 9, 1346–1358, Sep. 1996.
21. Figueiredo, M. A. T., R. D. Nowak, and S. J. Wright, "Gradient projection for sparse reconstruction: Application to compressed sensing and other inverse problems," *IEEE Journal of Selected Topics in Signal Processing*, Vol. 1, No. 4, 586–597, Apr. 2007.
22. Hale, E. T., W. Yin, and Y. Zhang, "Fixed-point continuation for L_1 minimization: Methodology and convergence," *SIAM Journal on Optimization*, Vol. 19, No. 3, 1107–1130, Oct. 2008.
23. Beck, A. and M. Teboulle, "A fast iterative shrinkage-thresholding algorithm for linear inverse problems," *SIAM Journal on Imaging Sciences*, Vol. 2, No. 1, 183–202, Mar. 2009.
24. Wright, S. J., R. D. Nowak, and M. A. T. Figueiredo, "Sparse reconstruction by separable approximation," *IEEE Trans. Signal Processing*, Vol. 57, No. 7, 2479–2493, Jul. 2009.